Numerical Study of Integrated Micro Ring Resonator and Micro Lens

by

Xiaopeng Guo

A thesis submitted in partial fulfillment
of the requirements for the degree of
Master of Science in Engineering
(Electrical Engineering)
in the University of Michigan-Dearborn
2018

Master's Thesis Committee:

Associate Professor Yasha Yi, Chair
Professor Weidong Xiang
Assistant Professor Joe Fu-Jiou Lo

Acknowledgements

First and foremost, I would like to avail myself of the opportunity to express my gratitude to Professor Yi, for his insightful guidance and enthusiastic encouragement in the researching process, without the consistent and valuable reference materials, this thesis would not have been possible completed.

Second, I would like to extend my heartfelt thank to my lab mate, Ye Mao, Dachuan Wu, Wei Guo and Yuheng Peng, who have contributed their time, thoughts, skills and encouragement to this thesis.

In the end, I also grateful to all the people who have given me generous support and helpful advice in the past few years.

Table of Contents

List of Figures

Chapter I Introduction and Basic Theory of Integrated Ring Resonator and Micro Lens

1.1 Introduction

Integrated ring resonator has generated wide interests in the detection and sensing field. The ring resonator is consisting of waveguides where one waveguide is a closed loop, and it will couple the light input and output. And now this photonic device has been widely used as optical sensor and filters in the telecommunications, biomolecule and biomedicine field.

And now the integrated micro resonators are investigated and utilized by many research groups. The most application of micro ring and micro lens can be fabricated in CMOS compatible microelectronic process.

1.2 Basic Theory of Ring Resonator

The basic single polarization ring resonator structure is shown as figure 1.1, the radius of ring resonator is r, assuming that mode of the resonator is single unidirectional and the coupling is lossless.

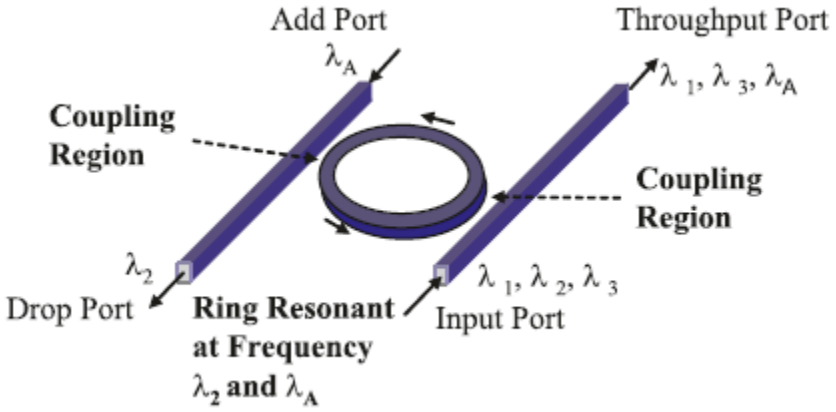

Figure 1.1 Ring resonator channel dropping filter

The attenuation constant can be expressed the various kinds of losses occurring along the propagation of light and can be described by the following:

$$\begin{pmatrix} E_{t1} \\ E_{t2} \end{pmatrix} = \begin{pmatrix} t & \kappa \\ -\kappa^* & t^* \end{pmatrix} \begin{pmatrix} E_{i1} \\ E_{i2} \end{pmatrix}.$$

The E are normalized, and that their squared magnitude corresponds to the modal power.

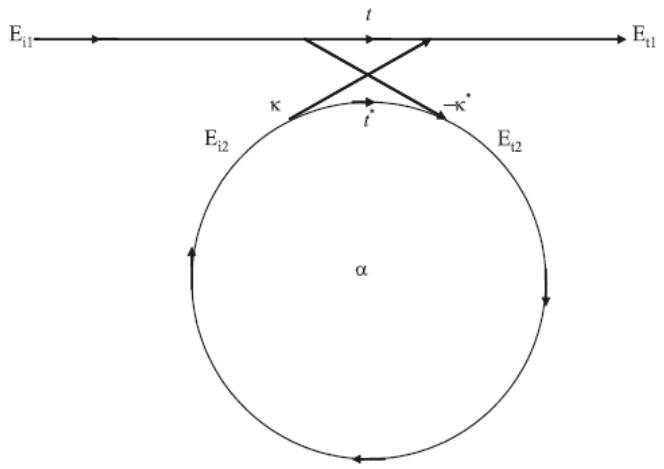

Figure 1.2 Model of a single ring resonator with one waveguide

The t and k are the coupler parameters, and usually the * denotes the conjugated complex value of t and k, respectively.

The matrix is symmetric because the networks under consideration are reciprocal. Therefore

$$|k^2| + |t^2| = 1 \tag{1.1}$$

To further simplify the model, E_{i1} is picked to be 1. Then the round trip of the ring is given by

$$E_{i2} = a * e^{j\theta} * E_{t2} \tag{1.2}$$

Where the a is the loss coefficient, $e^{j\theta}$ express the phase change in one round trip.

Thus the E_{i2}, E_{t1}, and E_{t2} can be solved:

$$E_{i1} = 1 \tag{1.3}$$

$$E_{t1} = \frac{-a+t*e^{-j\theta}}{-a*t+e^{-j\theta}} \tag{1.4}$$

$$E_{i2} = \frac{-a*k^*}{-a*t^*+e^{-j\theta}} \tag{1.5}$$

$$E_{t2} = \frac{-k^*}{1-a*t^**e^{-j\theta}} \tag{1.6}$$

In the thesis paper, all experiment part is totally done by simulation environment, and that means there no absorption and isotropic are considered. Thus, the one ring resonator with one waveguide is not valuable. Another basic model of ring resonator is adding an extra slab waveguide at the other side, shown in figure 1.3 and figure 1.4.

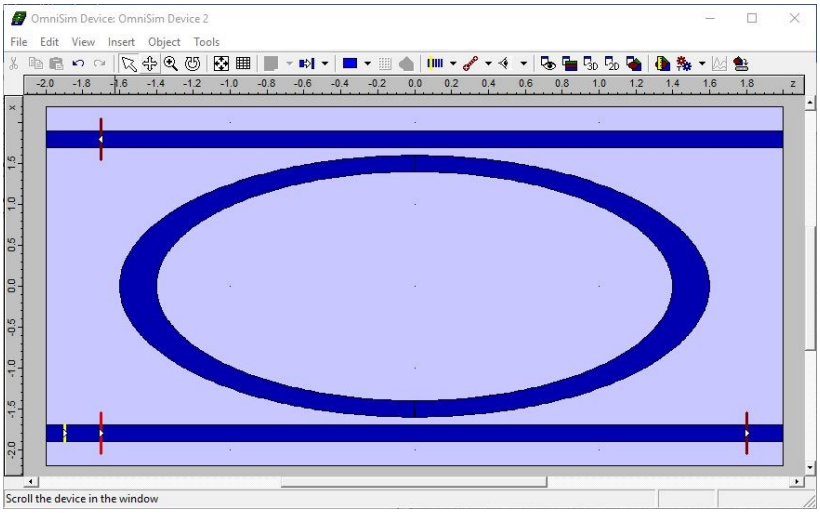

Figure 1.3 Ring resonator consists of one ring and two slab waveguides

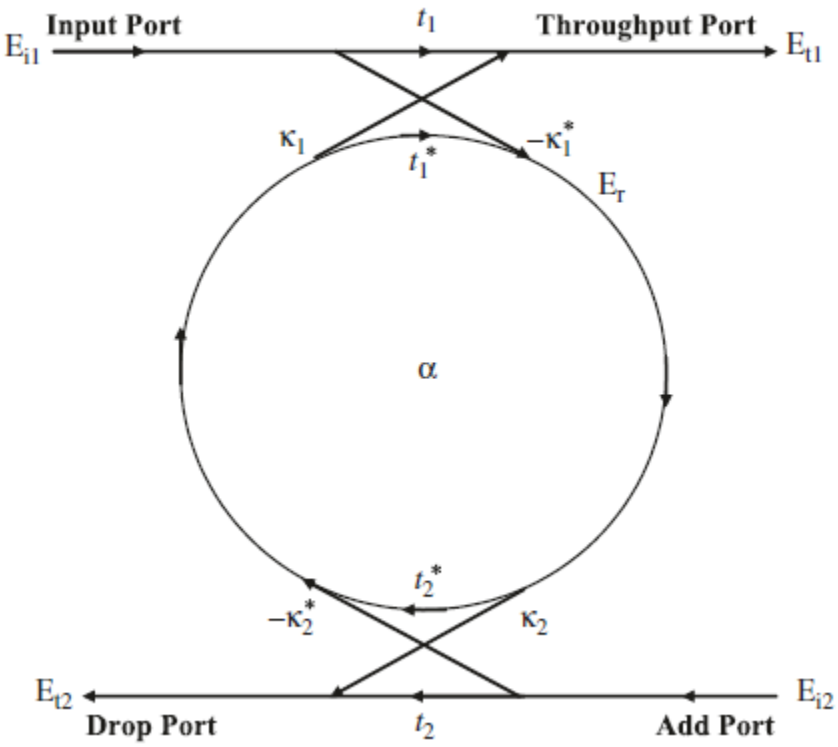

Figure 1.4 Model of a basic add-drop single ring resonator

And the coupling coefficient between input waveguide, output waveguide and ring both follow the equation (1.1), what's more, the t1 and k1, t2 and k2 in the figure 1.4 are equal to each other.

And assuming $E_{i1} = 1$, $E_{i2} = 0$, a=$a_{1/2}{}^2$, $\theta = 2 * \theta_{1/2}$, and the following will get:

$$E_{i1} = 1 \tag{1.7}$$

$$E_{t1} = \frac{-a*t_2{}^**t_1+e^{-j\theta}}{-a*t_2{}^**t_1{}^*+e^{-j\theta}} \tag{1.8}$$

$$E_{i2} = 0 \tag{1.9}$$

$$E_{t2} = \frac{-a_2*k_2{}^**k_2*e^{-j\theta}}{-a*t_1{}^**t_2{}^*+e^{-j\theta}} \tag{1.10}$$

The energy equations are the following:

$$P_{i1} = 1$$

$$P_{t1} = \frac{(|t_1| - a^2 * |t_1|)^2}{(1 - a * |t_1 t_2|)^2} \tag{1.11}$$

$$P_{t2} = \frac{a^2 * (1 - |t_1|)(1 - |t_2|)^2}{(1 - a * |t_1 t_2|)^2} \tag{1.12}$$

In the simulation environment, we set the a=1, although it can only be achieved by the implementation of gain incorporated in the ring resonator to compensate the waveguide losses. A possibility of achieving minimum intensity ($P_{t1} = 0$) at resonance of the output transmission. So, we can get

$$\mathrm{a} = \left|\frac{t_1}{t_2}\right| \tag{1.13}$$

However, the speed of EM wave in the waveguide is fast, the change of medium is small. When adding a ring resonator, the property of ring resonator can also be roughly explained by the concept of constructive interference. So, when the light crosses the ring resonator, and the wavelength follow the equation to resonance occurs.

$$n_{eff} * L = m * \lambda \tag{1.14}$$

Where n_{eff} is the effective refractive index of ring waveguide, L is the length of the light path inside the ring, which approximately equals to the circumference of the ring, m is an integer, and λ is the wavelength in vacuum of the EM wave. The wavelengths described by this equation is what we call the resonance wavelength or coupling wavelength.

Ring resonators can be described by the following general definition and equation.

FSR: the distance between resonance peaks, which is called the free spectral range

$$\mathrm{FSR} = \Delta\lambda \approx \frac{\lambda^2}{n_{eff} \cdot L} \tag{1.15}$$

FWHM: the resonance width which is defined as the full width at half maximum

$$\mathrm{FWHM} = 2\delta\lambda = \frac{k^2\lambda^2}{\pi L n_{eff}} \tag{1.16}$$

F is the finesse of the ring resonator, usually it can be described by the ratio of the free spectral range and the full width at half maximum:

$$\mathrm{F} = \frac{FSR}{FWHM} = \frac{\Delta\lambda}{2\delta\lambda} \approx \frac{\pi}{k^2} \tag{1.17}$$

The quality factor Q can measure the sharpness of the resonance

$$\mathrm{Q} = \frac{\lambda}{2\delta\lambda} = \frac{n_{eff}\cdot L}{\lambda} \cdot F \tag{1.18}$$

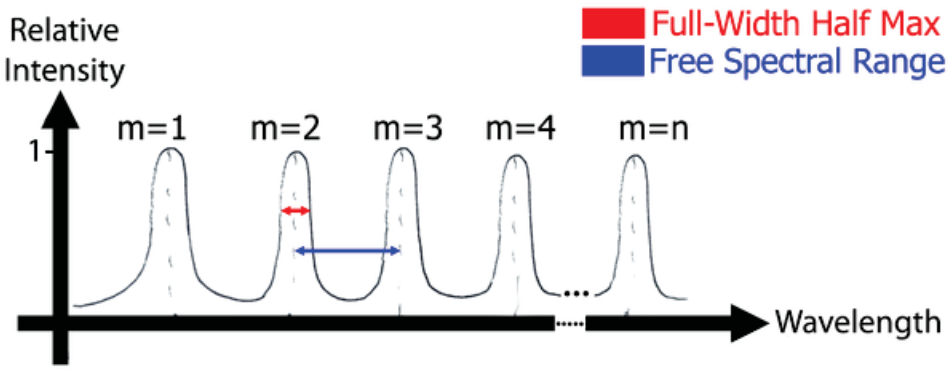

Figure 1.5 Illustration of Free Spectral Range and Full-Width Half Max

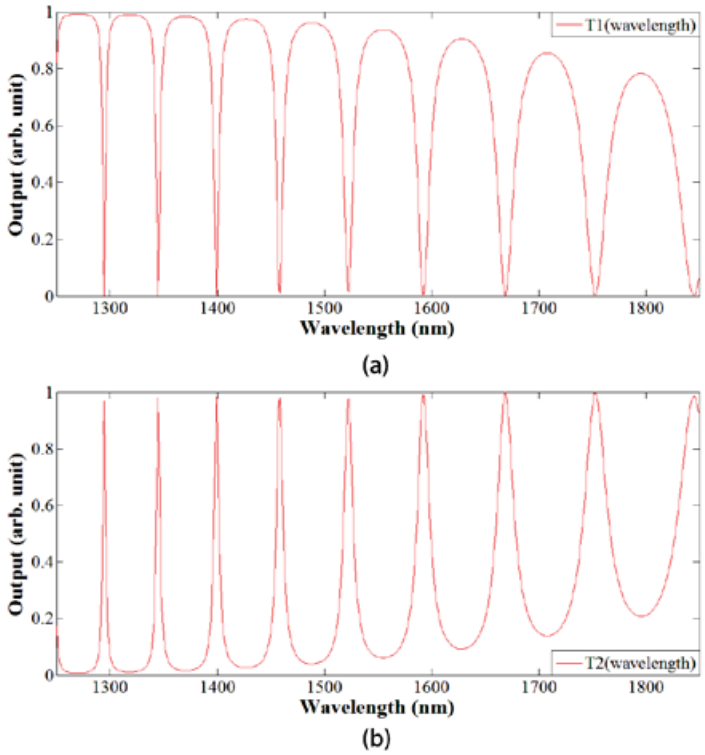

Figure 1.6 Transmission Spectrum of the Ring resonator(a)T1port(b)T2 port

The figure 1.6 shows the simulation result of the ring resonator in figure 1.3. The figure 1.6(a) shows the spectrum of throughput port, which is named as T1 in figure 1.4. The figure 1.6(b) shows the spectrum of drop port, which is named as T2. Compared these two peaks, the T1 are downwards, and T2 are upwards. Those conclusions agree the equation 1.14: wavelength fits the coupling condition propagate through the ring waveguide to output port, and the rest are remained in input port.

1.3 Basic Theory of EM Wave

The electromagnetic wave (EM wave) is shown in figure 1.7, the distribution of electrical field, magnetic field and the direction of propagation are perpendicular to each other.

And the Maxwell's equations can describe the behavior of EM wave.

$$\text{Gauss's Law: } \nabla \cdot \mathrm{E} = \frac{\rho}{\varepsilon_0} \tag{1.15}$$

$$\text{Gauss's Law for magnetism: } \nabla \cdot \mathrm{B} = 0 \tag{1.16}$$

$$\text{Maxwell-Faraday equation: } \nabla \times \mathrm{E} = -\frac{\partial B}{\partial t} \tag{1.17}$$

$$\text{Ampere's circuital law: } \nabla \times \mathrm{B} = \mu_0 (J + \varepsilon_0 \cdot \frac{\partial E}{\partial t}) \tag{1.18}$$

Where ε_0 is the permittivity of free space, μ_0 is the permeability of free space, ρ is electric charge density, and J is the electric current density.

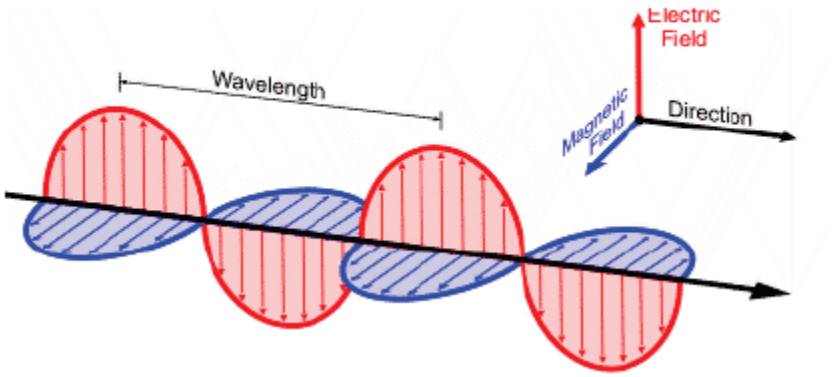

Figure 1.7 Illustration of Electromagnetic Wave

The propagation of EM wave is affected by two main parameters of medium: permittivity ε_0 and permeability μ_0. The waveguide is a structure designed to limit the propagation of EM wave shown in figure 1.8. And the refractive index of waveguide layer is larger than medium so EM wave would suffer total internal reflection while limited inside the waveguide layer.

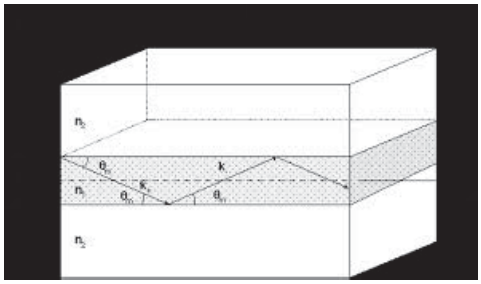

Figure 1.8 the Planar Waveguide

1.4 Basic Theory of Micro Lens

1.4.1 Introduction

The nanoscale subwavelength grating structure has been investigated widely as it promises a series of applications in integrated nanophotonic. In previous studies, low-contrast gratings, such as zero-contrast gratings (ZCG) based on guided-mode resonance structures and high-contrast grating were investigated as wideband reflectors. These types of subwavelength structures have the potential to be utilized in many applications including optical filters, sensing, and photodetectors, while offering flexible tunability of resonance wavelength and a high Q-factor. Until recently, nanorod arrays with high aspect ratios have attracted wide attention for their potential application into areas such as antireflection, self-cleaning, and super hydrophobicity. These subwavelength grating structures can be fabricated by various template-assisted etching fabrication techniques. A dry etching technique is one of the most favorable methods due to its excellent controllability and compatibility with the complementary metal–oxide-semiconductor (CMOS) technology. Both vertical and transverse etchings in most dry etching processes, such as the reactive-ion-etching technique, normally require a good control of the etching rate to achieve designed selectivity over underneath thin film.

Concentrating lenses are one of the most important applications of subwavelength grating structures. Various micro lenses, ranging from the traditional dielectric lenses to plasmonic lenses, have been designed based on the coupled-wave diffraction method. Among all such micro lenses, the subwavelength structure designs based on recently proposed HCG structures have gained the most attention on account of their compatibility with planar CMOS integration processes while

retaining excellent light focusing properties.

In this study, we discovered the existence of a threshold in grating thicknesses, where the light concentration property of the grating lenses spikes drastically upon breach. This effect is hypothesized to be the consequence of the formation of a complete concentration mode inside each bar, which significantly facilitates the mode interference between adjacent bars. Moreover, steadily varying the grating thickness yielded the discontinuous change in the focus property, which may indicate that the mode confined inside the grating (i.e., light trapping) maybe subject to a self-interference effect along the light propagation direction.

1.4.2 Zero-Contrast Gratings Subwavelength Grating Structures

ZCG subwavelength grating structures are shown in Fig. 1.9. As shown in Fig. 1.9, the gratings are composed of silicon nitride (Si_3N_4 with a refractive index of 2); each bar has a different bar-width (S_0; $S_{1...}S_N$) and has varied airgaps (A_0;A_1;...,A_N) between adjacent bars. Both the bar-width and airgaps are designed to achieve a concentration effect; the bar-width is varied from 180 to 80 nm, while the airgap is varied from 170 to 60 nm. The relationship of S_N and A_N is designed such that the light passes through the gratings in the same phase on the focus. That is, for each bar S_N, the phase remains $\emptyset(x)$, where y is the focal length given as

$$\emptyset(x) = 2n\pi + \frac{2\pi f}{\lambda} - \frac{2\pi\sqrt{f^2+x^2}}{\lambda} \tag{1.19}$$

The waveguide layer shown in Fig.1.9 for ZCG is a waveguide layer which is typically naturally formed through the dry etching method and consists of the same material as the grating layer (Si_3N_4 in this study). The ZCG structure is created by adding a waveguide layer with the same material as the gratings; the refractive index difference between the gratings and the bottom waveguide layer is zero. Glass, which is considered as a homogeneous material with a refractive index of 1.48, is chosen as the substrate layer.

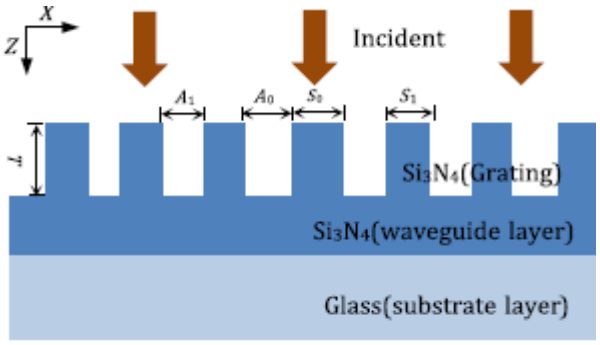

Figure 1.9 Zero-contrast grating

1.4.3 Simulation Methods

Numerical analysis of the light concentration characteristics and electromagnetic (EM) field distribution is performed using the finite-difference-time-domain simulations. A TM polarized broadband planewave source (750 nm) is launched in the positive direction of the z-axis and interacts with the subwavelength structure. Perfect matched layers boundary conditions are placed above the top and below the bottom boundaries of the simulation window such that the vertically transmitted and reflected EM waves are absorbed.

Several detectors are placed below the structure to collect the transmitted light. In order to observe the EM field distribution at certain wavelengths, a monochromatic EM plane wave is launched normally at the desired wavelength; the EM intensity in the structure is then recorded. A fine grid of size 5 nm, together with a sufficiently long duration time, is used to conduct the simulation. Detailed simulation results

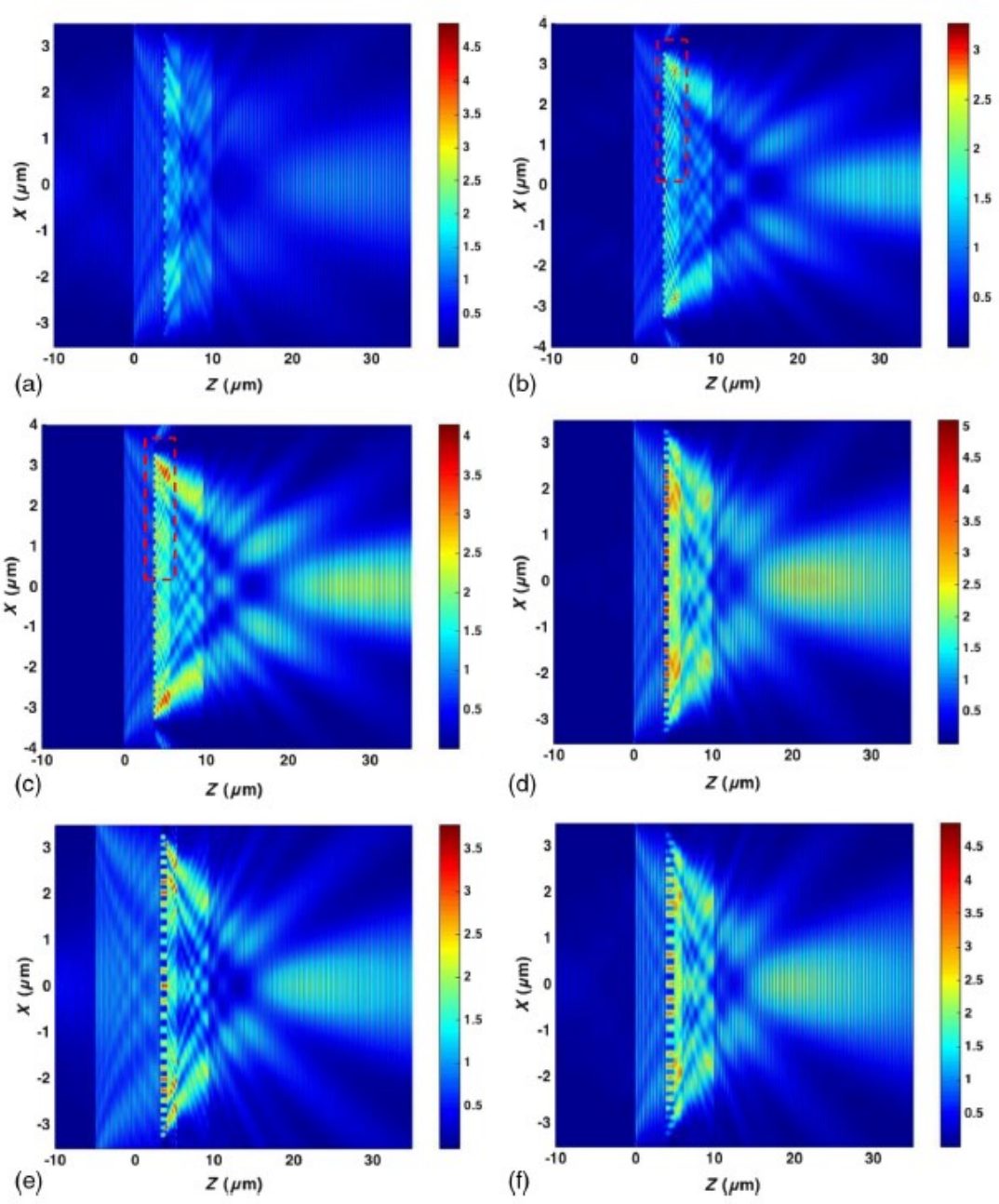

Fig. 1.10 (a) Field distribution at 750-nm source of 200-nm grating thickness. (b) Magnetic field distribution at 750-nm source of 250-nm grating thickness. (c) Magnetic field distribution at 750-nm source of 300-nm grating thickness. (d) Magnetic field distribution at 750-nm source of 600-nm grating thickness. (e) Magnetic field distribution at 750-nm source of 800-nm grating thickness. (f) Magnetic field distribution at 750-nm source of 1000-nm grating thickness.

Chapter II Ring Resonator Based Methane Sensor

2.1 Introduction

It's well-known that alkanes, especially the methane, even if the concentration is low, it is a compound very dangerous to human safety and the environment. The earliest gas detection sensor is electrical sensor. The Electrical sensors through the over-sensitive components covert the gas concentration to electrical parameters for transmission.

Several measurement techniques were previously used for development methane sensor. Traditionally, metal oxide films are used as a gas sensitive material. These sensors worked based on the principle of semiconductor surface conduction of sensors changes in relation to the absorption of the target gas like methane.

A fiber core methane sensor ring resonator based on the change of refractive index, especially applied on the ordinary fiber is stated in this chapter. This methane sensor detects the changes in the output light intensity to calculate the refractive index through the photodetector, resulting in methane concentration.

2.2 Basic Model and Simulation

2.2.1 Single Ring Model

The basic model in this thesis simulation is shown in figure 2.1, the ring resonator parameters are: the diameter of ring waveguide is 3000nm, which is coupled with two straight waveguides. The light path is input from the left bottom corner and collect from the right top corner of the slab waveguides. In order to keep the single waveguide mode condition, these slab waveguides both

have a width of 200nm. The red layer is cryptophane-A material, which will introduce in the next paragraph, the width is 500nm deposited in the inner surface of the ring resonator. The gap between the ring and the straight waveguides is 100nm. Because the critical coupling condition of the ring resonator without the inner layer is close to 100nm, and the coupling gap also depends the coupling power.

The blue layer is the main material silicon (Si), the refractive index of Si is 3.48, notes that in this thesis simulation the wavelength is limited in the 1500-1600nm, the bottom cladding is SiO2 with refractive index 1.45 in 3D model.

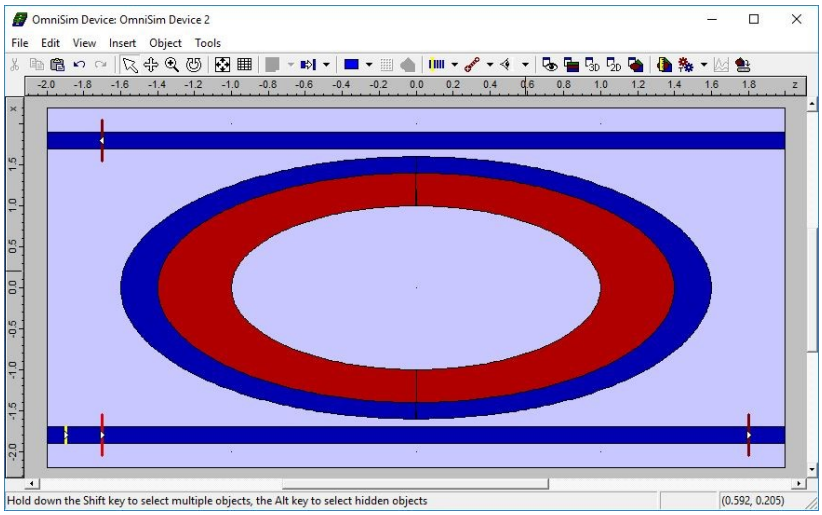

Figure 2.1 the top view of the methane-sensitive material cryptophane-A layer coating

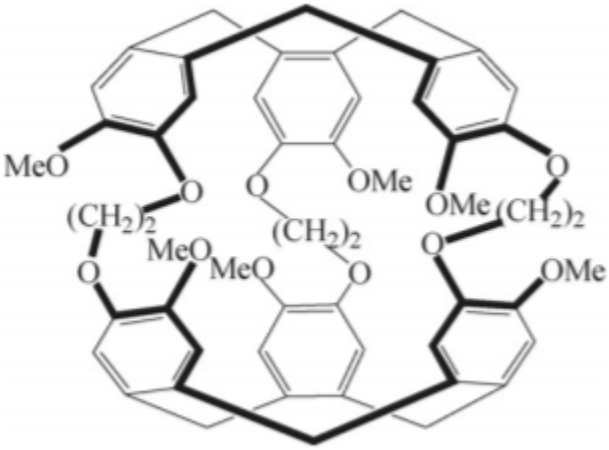

Figure 2.2 Chemical structure of cryptophane-A

The basic theory of the methane sensor is the cryptophane-A is equivalent to micro ring's cladding, when methane reacts with it, will cause an obvious refractive index change. That also cause the effective refractive index the propagation mode changes, eventually causing resonance wavelength shift. The process is such like the figure 2.3.

The studies have shown that cryptophane-A has a strong affinity for methane and at last 6 months stability. Based on this, this thesis used it as the ring resonator sensitive layer. When the sensitive layer is in contact with methane, the methane molecules expand disperses into the interior of cryptophane-A layer and interacts with non-covalent interactions, and selectively enter the hole in cryptophane-A molecule, cause the refractive index of the layer changes, thus the effective refractive index of the micro ring resonator changes and the resonance wavelength shifts. Studies also have shown that the refractive index of cryptophane-A increases with the increase of the methane concentration, as the figure 2.4 shown. The refractive index n of the film is almost linear with the methane concentration C, the slope is 0.053.

$$n = 0.053C + 1.412 \tag{2.1}$$

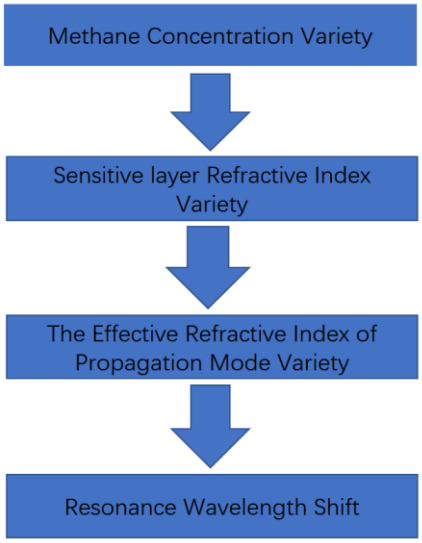

Figure 2.3 the Basic Theory of Ring Resonator Based Methane Sensor

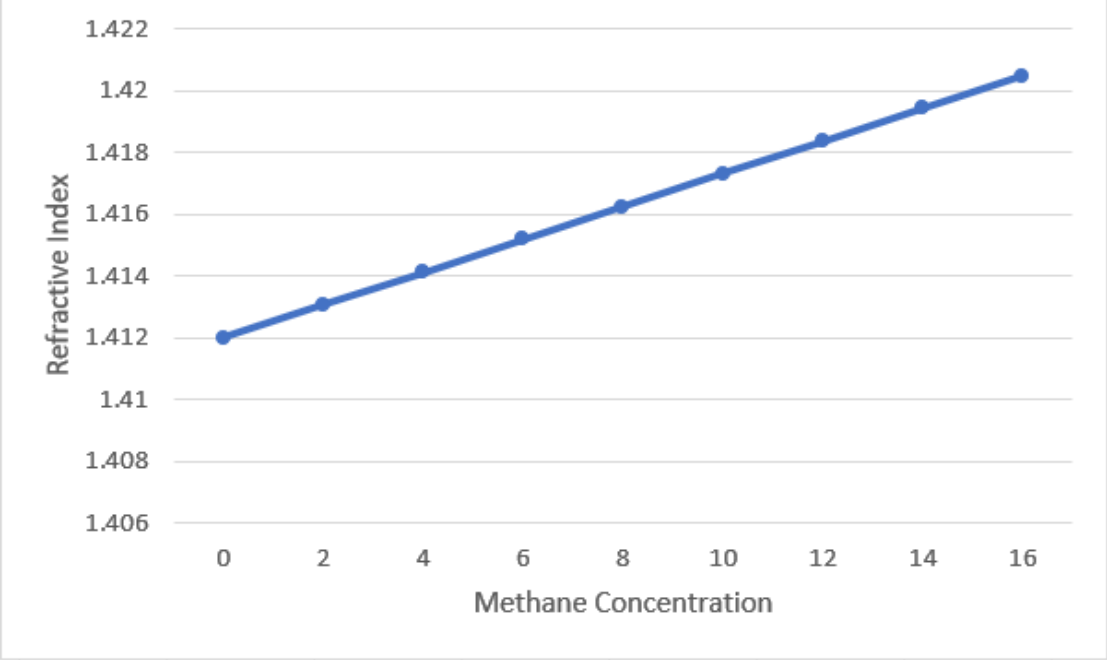

Figure 2.4 The Relationship between the Cryptophane-A Refractive Index and Methane Concentration

The concentration of methane in the surrounding environment increases, the n_{eff} will change according to the change in the refractive index of cryptophane-A layer. For example, the refractive index of cryptophane-A at wavelength 1550nm is n=1.412, $\alpha = 0.001$, where the n is the real part and α is the imaginary part. In the 0% to 12% range, the change of the refractive index is almost linear to the variation in the methane concentration.

This simulation is applied to our FDTD simulation. The boundary condition is the perfect matched layer, also called PML, the FDTD grid size is 20nm, and the input signal is a wavelength range 1500nm to 1580nm sinusoidal pulse. Also, the long evolution time steps are necessary to ensure the precision and resolution of the results. This part will main introduce the half cover of cryptophane-A layer.

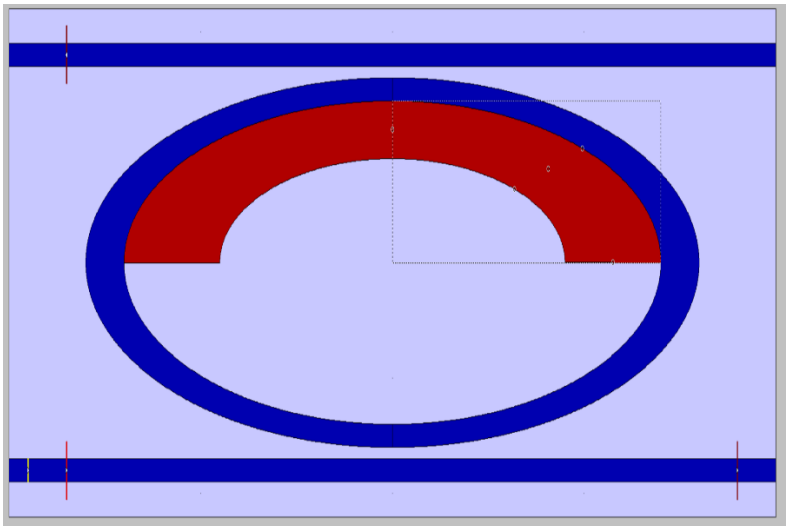

Figure 2.5 Top View of the Ring Resonator with Half Cover Cryptophane-A

The figure 2.6 shows the resonance wavelength shift between 1520 to 1530nm for cryptophane-A coated micro ring resonators when methane concentration is increased from 0% to 12%. As the figure 2.6 shown, the resonance wavelength has shift of approximately 0.017 nm (i.e., 0% methane resonance wavelength is 1.524042 um, and 2% methane resonance wavelength is 1.524058 um).

From the above result, the integrated micro ring resonator methane sensor can detect changes in methane concentration from the resonance wavelength shift using precision spectrometer. The relationship between the resonance wavelength and the methane concentration is

$$\lambda = 1.5240 + 1.7 * 10^{-7} C \quad (2.2)$$

This method has less requirements on the incident angle and refraction angle to the fiber and avoid the light loss at the intersection of single mode fiber and multimode fiber or the bend. That will be resulting in light intensity due to the lack of fiber itself collapse and weaken, affecting the detection accuracy. Due to the ultra-small size of the micro ring resonator structure, the resonance wavelength change is at least one order of magnitude larger than the optical fiber-based methane sensor.

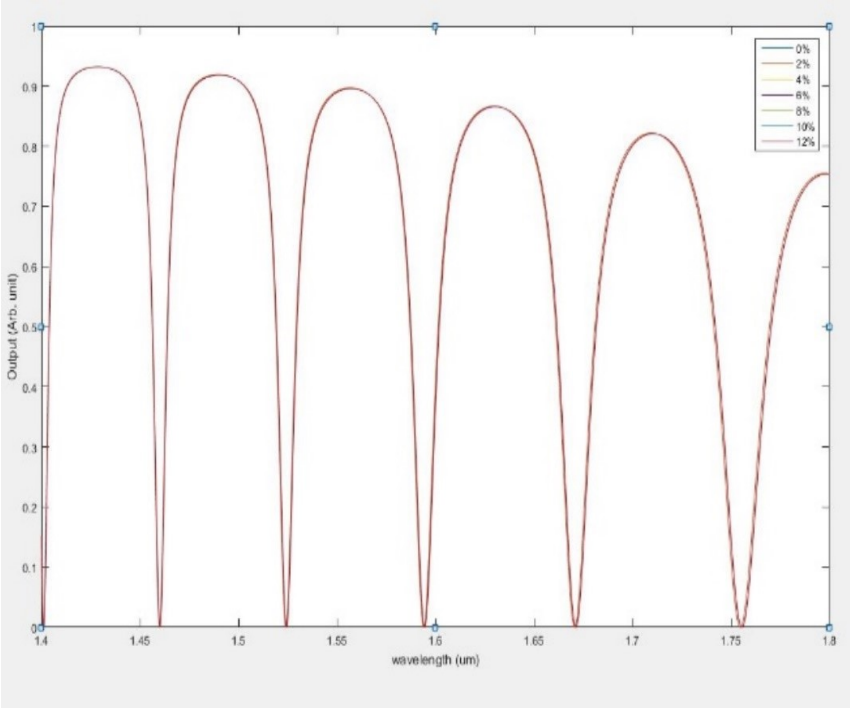

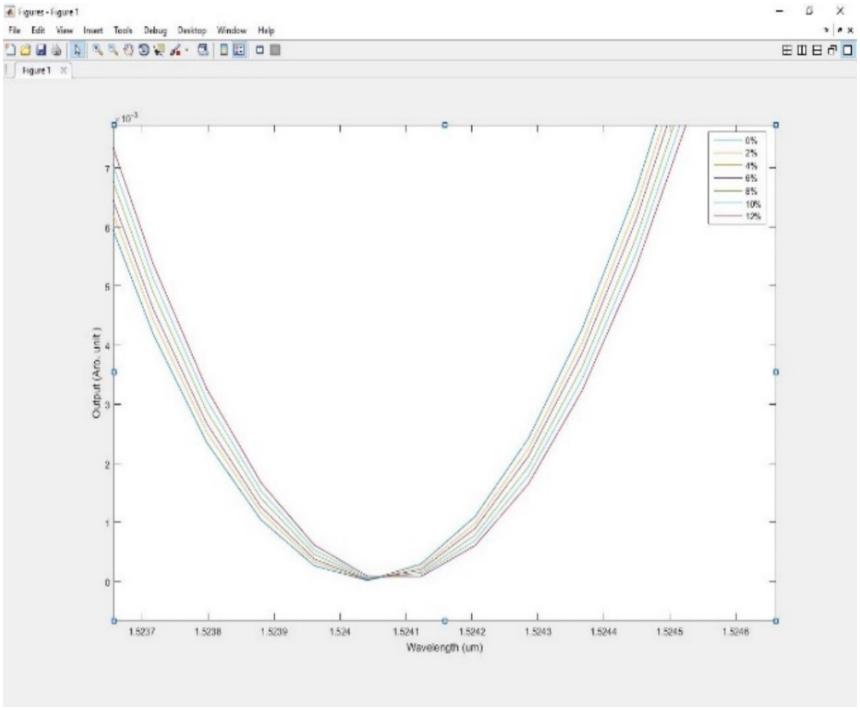

Figure 2.6 the Resonance Wavelength shift of the half-Covered Ring resonator with methane concentration variation from 0%~12%.

2.2.2 Investigation of the Coverage Proportion of Cryptophane-A

As the result shown, the real part n of the refractive index determines the resonance wavelength shift because of the methane concentration changed. That exists a tradeoff between the resonance wavelength and the resonance mode quality factor (Q), we can assume that if there is more coating of cryptophane-A layer, there may have more wavelength shift for the higher Q. Therefore, the cover proportion of Cryptophane-A layer is necessary to investigate further.

The cover proportion is investigated by simulation with four different structures, shown in the figure 2.7, the ring resonator coved with (a) one-fourth, (b) half, (c)three-fourth and (d)full with the methane-sensitive material cryptophane-A.

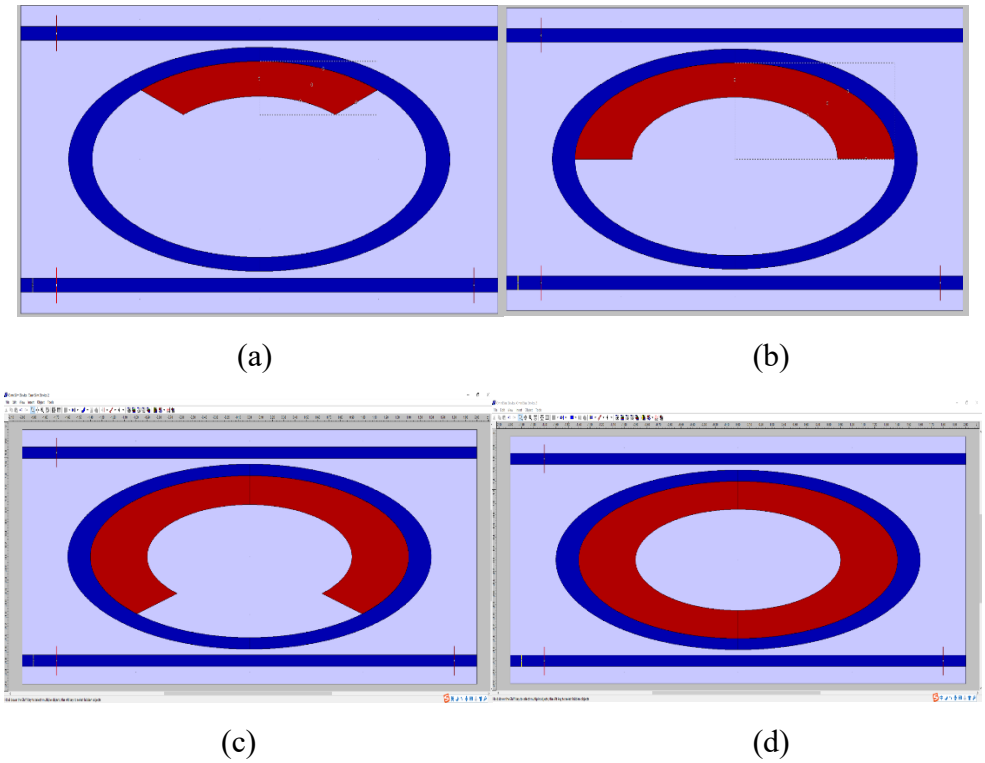

Figure 2.7 (a) one-fourth cover (b) half cover (c) three-fourth cover (d) full cover

Figure 2.8, 2.9, 2.10 and 2.11 show the simulation results of one-fourth, half, three-fourth and full covered cryptophane-A micro ring resonator structure, respectively.

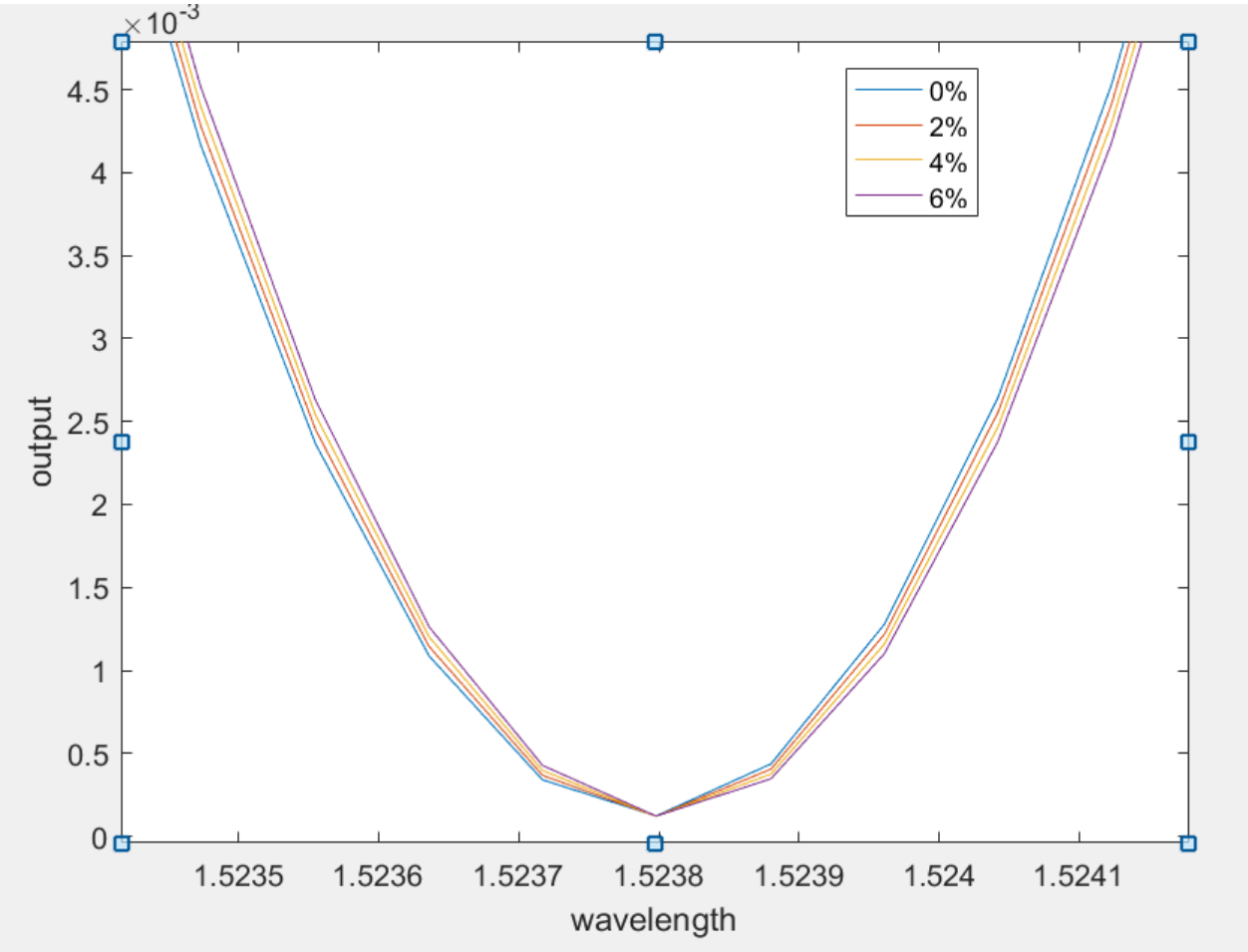

Figure 2.8 one-fourth-covered simulation result

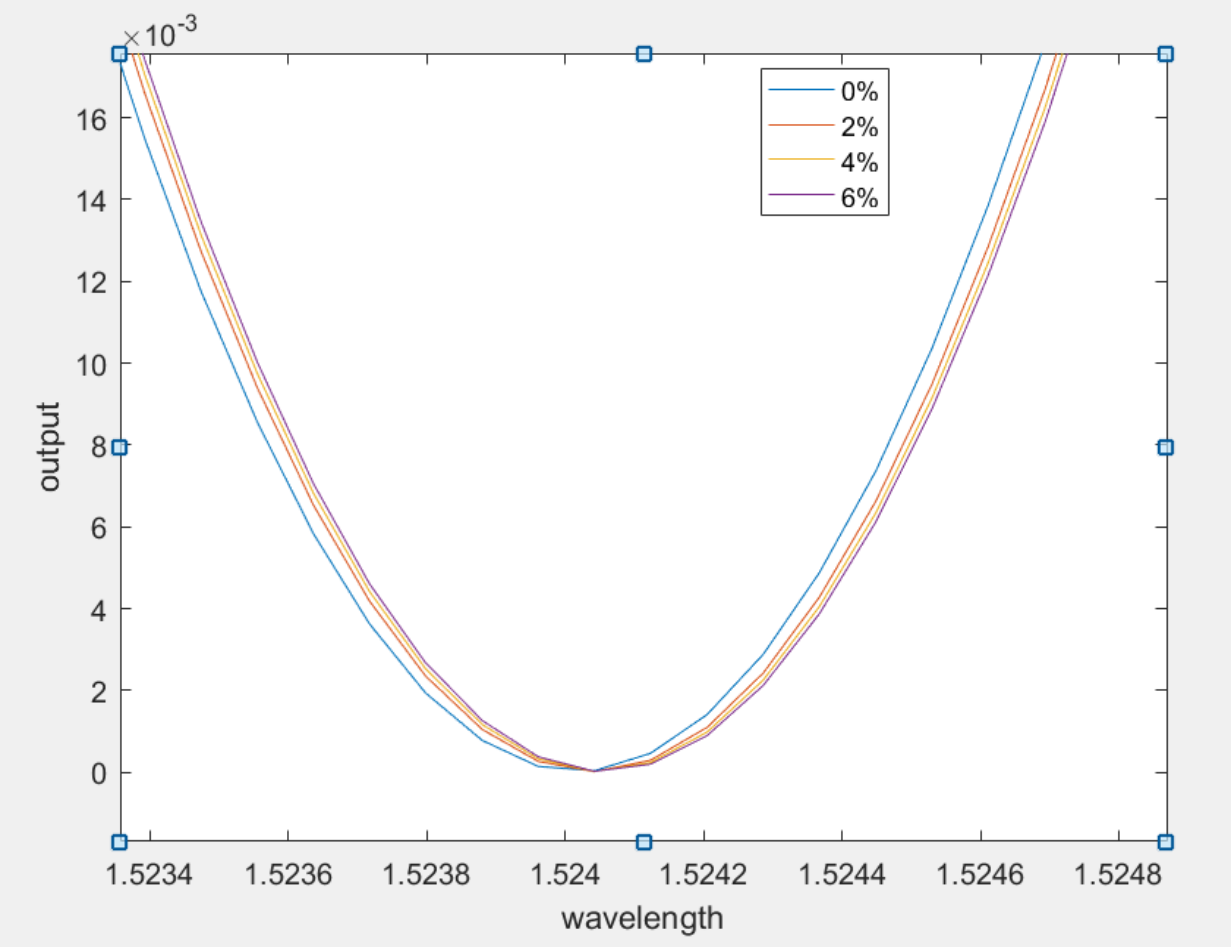

Figure 2.9 half-covered simulation result

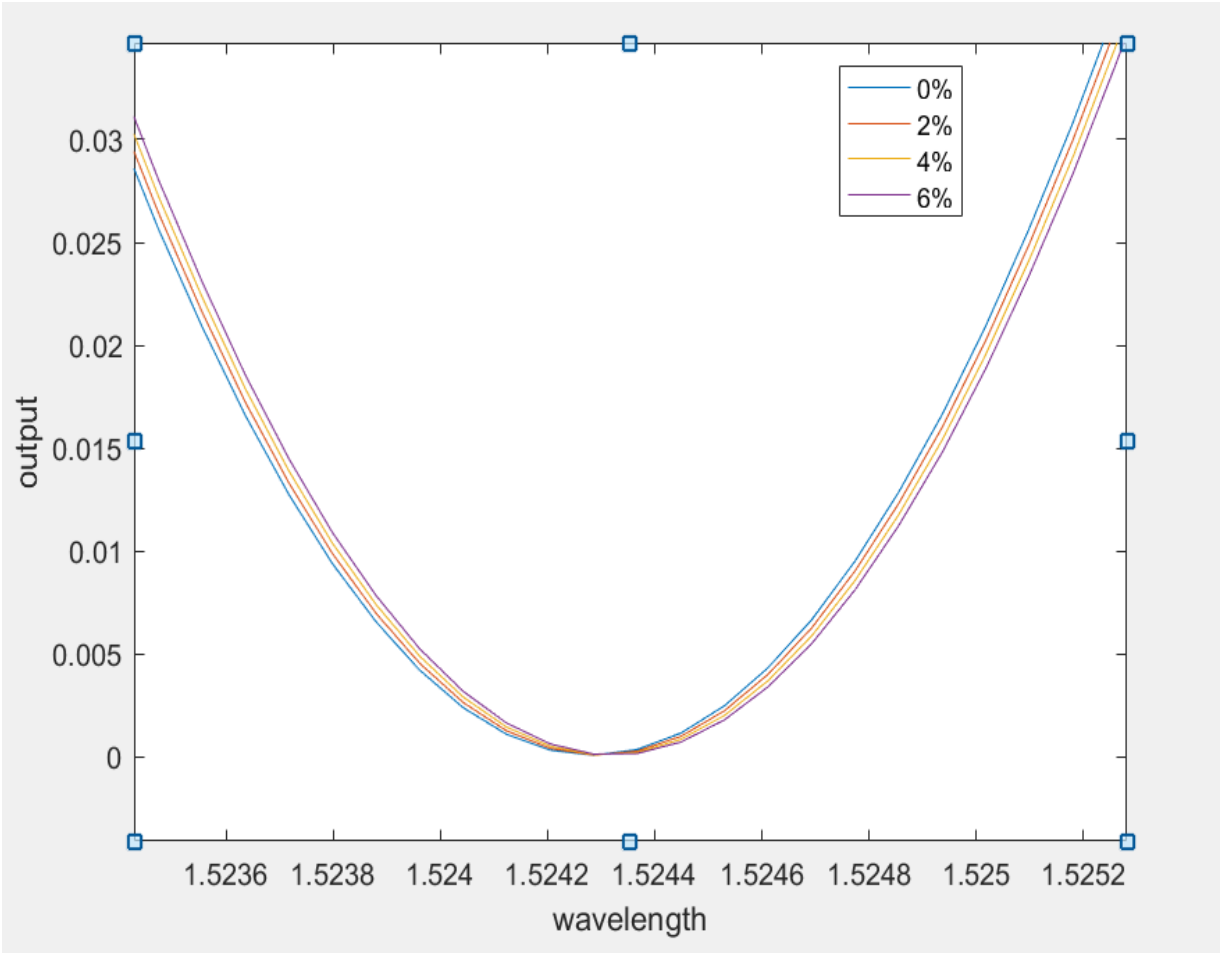

Figure 2.10 three-fourth covered result

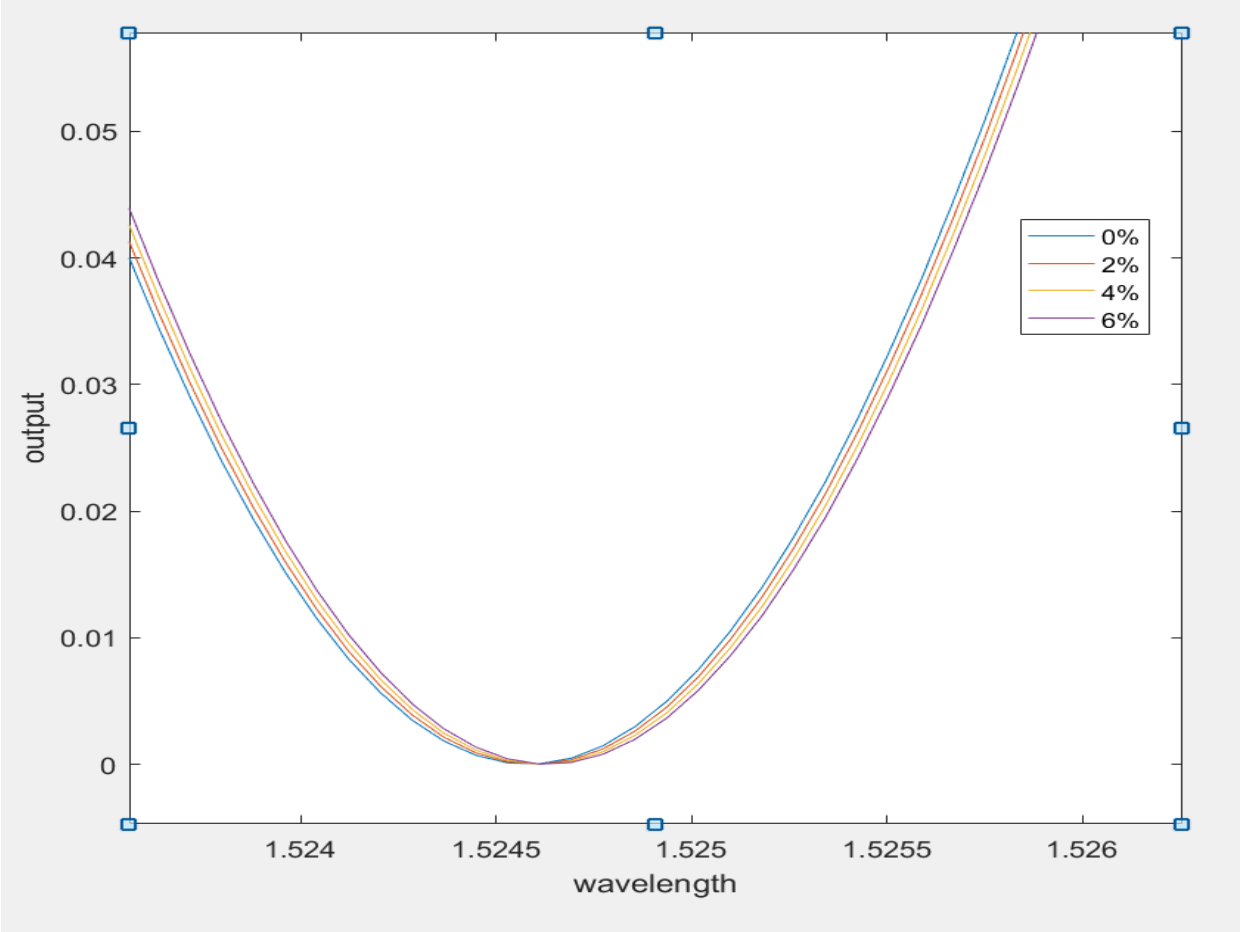

Figure 2.11 full covered result

The result can be clearly observed that a higher coverage proportion will contribute to a larger resonance wavelength shift. With 2% methane concentration increased, the resonance wavelength shift is: 0.008nm for one-fourth covered, 0.017nm for half covered, 0.032 for three-fourth covered and 0.066 for full covered.

This result can used be on the ultra-small micro ring resonator structure (um), and it is convenient applied in antenna. It avoids electromagnetic interference on methane sensor like catalytic and metal oxide sensors, electrochemical sensor and thermoelectric gas sensor. But it still need a high-resolution spectrometer on the output part to detect the wavelength shifts.

2.3 Double Cascaded Ring Structure

2.3.1 Introduction

Recently intense work has been devoted to the development of optical label-free biosensors, particularly the waveguide based evanescent field sensors due to their potential for high-sensitivity and suitability for implementing into an array format. The waveguide evanescent field sensors rely on monitoring the perturbation of the waveguide mode effective index n_{eff} due to the presence of an analyte in the solution that is in contact with the waveguide surface. An optical interference structure such as a Mach-Zehnder interferometer or an optical resonant structure such as a micro-ring resonator is commonly used. The latter can provide a higher sensitivity due to the sharp resonance peak. The effective index variation can be detected by wavelength interrogation or intensity interrogation for a fixed wavelength. With wavelength interrogation, the accuracy of the measurable effective refractive index variation is determined by $\delta n_{eff} = n_{eff}\delta\lambda/\lambda$, where $\delta\lambda$ is the wavelength accuracy limited by the measurement instrument. For $\delta\lambda$=0.01nm in the 1550nm wavelength region, δn_{eff} is in the order of 2×10^{-5}.

In this thesis, we investigate a new waveguide sensor based on two cascaded micro ring cavities of slightly different diameters, using the Vernier effect to gain the resonance wavelength shift. This can greatly increase the sensitivity of the effective refractive index and the resonance wavelength shift stated in the above part without using a high-resolution spectrometer.

2.3.2 Device Structure and Conclusion

The figure 2.12 and 2.13 shows schematic and simulation methane sensor, which consists of a reference ring A cascaded with a sensing ring B. The optical path lengths of these two rings are designed to be slightly different to employ the Vernier effect by choosing different radius (R_A and R_B). Thus, the free spectral ranges (FSR) is different for ring A and ring B, respectively.

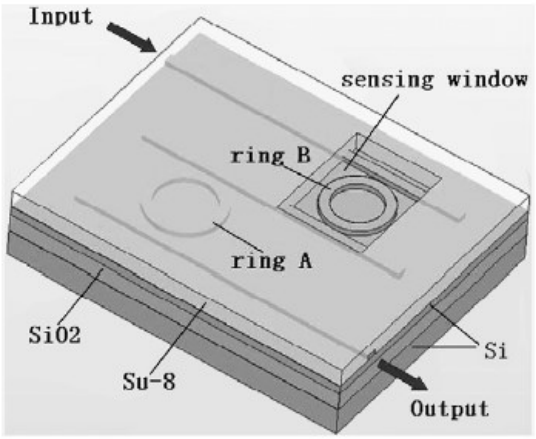

Figure 2.12 Schematic of the cascaded micro ring resonator sensor

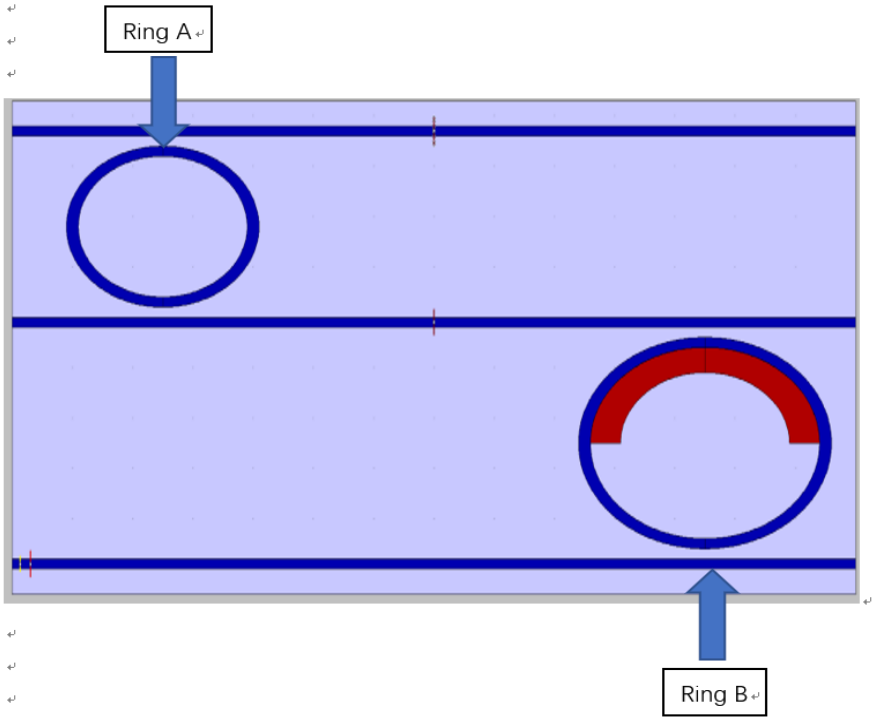

Figure 2.13 Simulation of the cascaded micro ring resonator sensor

To describe the principle of the two cascades ring sensor, the theory transmission spectra T_A and T_B for ring A and ring B are plotted in Figure. In our design, the $R_A < R_B$, where $R_A = 1.5\,um$, $R_B = 2um$, that means $\Delta\lambda_{FSRA} > \Delta\lambda_{FSRB}$. What's more, the total transmission spectrum T=$T_A \times T_B$, as shown in figure 2.14. The variation of refractive index of the cryptophane-A results in a change in the effective refractive index of ring B Δn_{eff}, and the change of resonance

wavelength is $\Delta\lambda_B = \lambda_B(^{\Delta n_{eff}}/_{n_{eff}})$, this is the wavelength shift data stated in the above part.

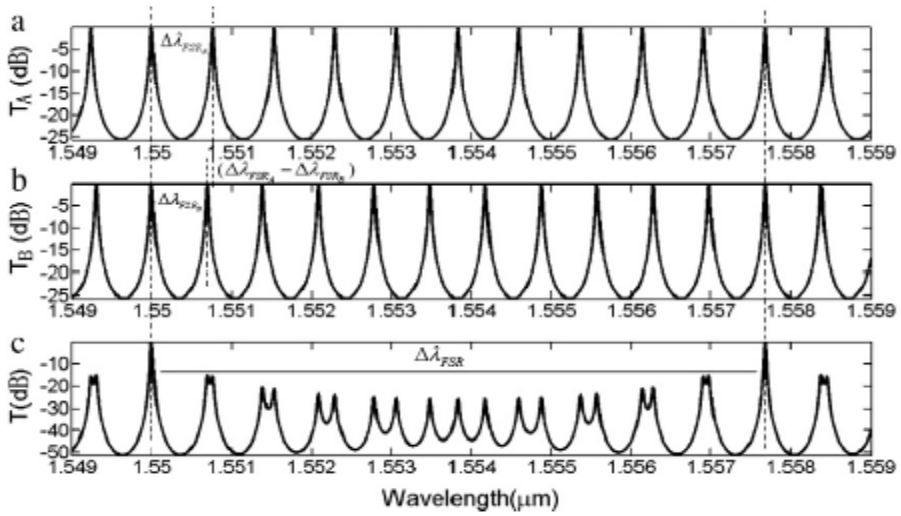

Figure 2.14 Theory transmission spectra of ring A (a) and ring B (b); and (c) total transmission spectrum.

And according to the Vernier effect, the total change $\Delta\lambda = \Delta\lambda_B \times [\Delta\lambda_{FSRA}/(\Delta\lambda_{FSRA} - \Delta\lambda_{FSRB})]$, this means the sensitivity of two cascaded rings resonator is gained by a factor of G=$\Delta\lambda_{FSRA}/(\Delta\lambda_{FSRA} - \Delta\lambda_{FSRB})$. As compared with the data in part 2.2, it has a more than 10^4 gain as figure 2.15 shown. The Figure 2.15 is half covered and 2% methane condition.

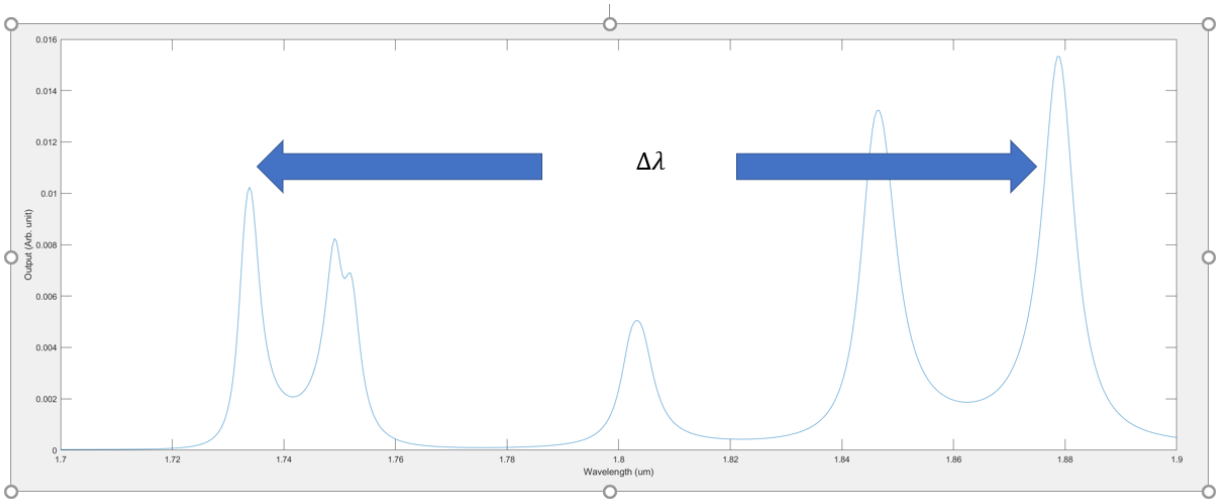

Figure 2.15 The simulation result of two cascaded ring with half covered and methane 2% concentration

Form the result, it can be clearly got that the detected wavelength shift $\Delta\lambda$ is about 147 nm,

compared with the same condition result (0.017nm) in part 2.2, the result has a 10^4 gain. Because of the simulation, the radius is not large as the theory value (more than 10 um), the result is not perfect as theory value (the single one ring transmission is shown in figure 2.16). But it also very straightforward performance the gain of this method. This can greatly increase the sensitivity of the effective refractive index and the resonance wavelength shift stated in the above part without using a high-resolution spectrometer.

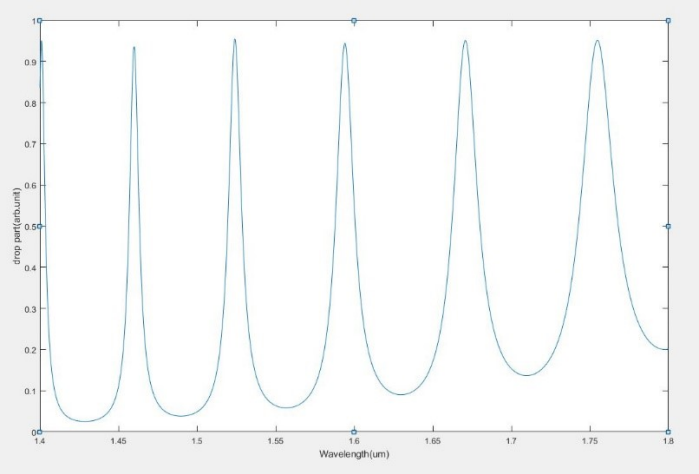

Figure 2.16 The real single one ring transmission

Chapter III Transmission Enhancement of Subwavelength Grating Micro Lens by Tapered Nano Structure (published)

3.1 Introduction

The emerging planar subwavelength micro lens have attracted wide attention recently. There exists a trade-off in selection of phase shifter materials for the lens designed with linearly polarized incidence. In this work, we have discovered that it is possible to utilize tapered nano structure to increase the transmission of phase shifters built with high refractive index materials. A typical grating micro lens is demonstrated to examine the effectiveness of taper-enhancement effect - the focus efficiency is increased from 9% to 28% with properly designed tapered sidewall. Our work will provide a novel method to enhance performance using high refractive index materials in the emerging micro lens field.

3.2 Basic Model and Simulation

Subwavelength micro lens is one of the emerging planar micro optical devices with great potential in a variety of applications. Among this field, high refractive index contrast nano structures shows great advantages in areas such as spectrally modification of optical wave front. These advantages have enabled the micro lens to be designed in a scale ranging from microns to several millimeters with focus size less than a micron.

The design of subwavelength micro grating lens follows a widely acknowledged phase matching process. Basically the micro grating lens is consisting of a group of phase shifters (e.g. subwavelength nano gratings defined by period and fill factor) that each of them will tune the phase of light (that pass through this phase shifter) based on its dimension and refractive index. To be specific, the phase profile of a typical focusing subwavelength grating lens is governed by the equation:

$$\phi(x) - \phi(0) = \frac{2\pi}{\lambda}\left(\sqrt{x^2 + f^2} - f\right) = -\Delta\phi \tag{3.1}$$

Where λ is the incident wavelength, f is the designed focal length, x is the distance between the phase shifter and the center of the lens, $\phi(x)$ is the phase needed for this phase shifter, and $\phi(0)$ is the phase at the center of lens. $\Delta\phi$ is the phase difference created by the nano structure at this location. For micro grating lens, necessary phase shifts (e.g. $\phi(x)$) can be acquired through different subwavelength nano structures (gratings) defined by period and fill factor (also known as duty cycle). In other words, the focusing subwavelength grating lens is designed by selecting appropriate grating structures to fulfill the phase profile of a focusing lens (e.g. eq. 3.1).

Based on the subwavelength nature of phase shifters, physical realization of the micro lens relies on nano fabrication techniques. To be specific, it can be either fabricated through reactive ion etching (top down process) or deposition then lift-off (bottom up process). Despite the difference in processes details, both of the two techniques have one common challenge that it is extremely difficult to fabricate structures with high aspect ratio (e.g. ratio higher than 5:1 thickness vs. width). For planar gratings lens that is designed under linearly polarized incidence (e.g. utilization of propagation phase not Pancharatnam-Berry phase), different phase shift is created by altering the equilibrium refractive index. In order to achieve enough phase shift in visible wavelength with limited thickness (e.g. low aspect ratio), researchers have looked into high refractive index material such as GaN and TiO_2. While high refractive index materials are enabling phase shifters more phase shift with comparatively low aspect ratio, their transmission may experience a significant drop.

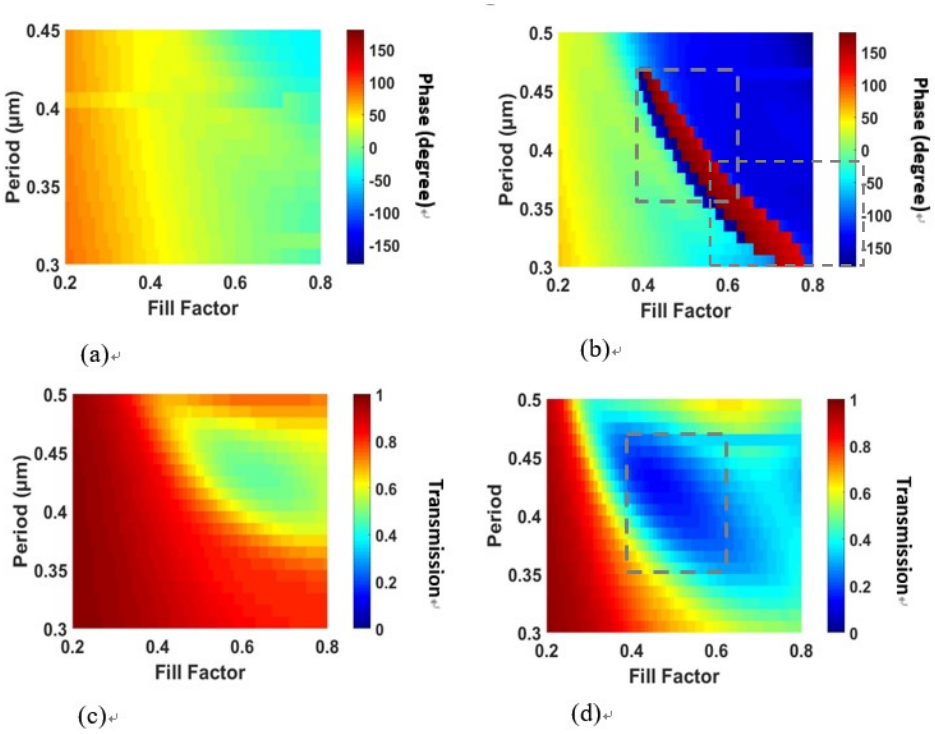

Figure 3.1 Phase diagrams and transmission for single phase shifters with thickness of 400 nm. (a) Phase diagram for Si_3N_4 phase shifter. (b) Phase diagram for TiO_2 phase shifter. (c) Transmission for Si_3N_4 phase shifter. (d) Transmission for TiO_2 phase shifter. The thickness of all phase shifters is fixed at 400 nm.

To compare the phase shift and transmission of high index and low index nano structures, we have chosen two materials as Si_3N_4 (refractive index 2.0) and TiO_2 (refractive index 2.55) and conducted the study through two dimensional finite different time domain method (FDTD) under light incidence of 685 nm, showed in Fig. 1. Nano structures in Fig. 1 are defined by period and fill factor (also known as duty cycle), and the dimensions presented here covers most conventional phase shifter dimensions in 2D domain. Perfect match layer (PML) is applied on boundaries (both ends) of incident direction to truncate simulation area. Periodical boundary condition is applied (on other 2 boundaries) for the extension of grating during the creation of phase map. Sufficiently long time steps and sufficiently small grid size are utilized to ensure the precision of FDTD simulation. The refractive index of air is set as 1 and the phase shifter is mounted on a glass substrate with refractive index of 1.5. The imaginary part of refractive index is neglected.

Showed in Fig. 3.1 (a) for a single Si_3N_4 phase shifter with thickness of 400 nm, the phase can

be shifted in a range of 68 degrees (0.37π) with the variation of nano structure dimensions (period from 0.3 to 0.48 μm, fill factor from 0.2 to 0.5). In comparison, TiO_2 counterparts (in same dimensions) can cover all phase shift (e.g. 360 degree), as showed in Fig. 3.1 (b). While the transmission rate for this group of TiO_2 phase shifters can be as low as 20% (Fig. 1 d), in sharp comparison with their Si_3N_4 counterparts with transmission above 80% for most of phase shifters shown in Fig. 3.1 c.

As a result, in order to design an optimum planar micro lens, one should either increase the phase coverage of low index material nano structures or increase the transmission of high index material nano structures. While the most effective way of increasing phase coverage of nano structures is to increase its thickness (increase single mode propagation length inside the structure). While this idea may not be practical, as we already approaching the limit of current nano fabrication with 80 nm of feature size and 400 nm of thickness. Upon realizing this, we have to consider through another direction as mentioned previously, that is to increase the transmission of high index material nano structures.

Moth eye is a subwavelength conical structure which is proved to have enhancement effect on transmission for high refractive index organic material (moth pupil). Recent study has mimicked the moth eye with subwavelength tapered structures in a more microscopic scale to achieve giant light extraction for high refractive index devices such as scintillators. On the other hand, the creation of tapered structure has long been considered as a side effect of reactive ion etching. The side wall taper is especially common during the etching of subwavelength micro lens structures as a number of nano structures (phase shifters) with a wide range of dimensions is etched at the same time. In addition, recent studies have achieved the controlled modification of nano tapered structure through reactive ion etching. To describe the dimension of tapered nano structure, the taper ratio b is defined as b= BTT/H showed in Fig. 3.2 (a), and a 2D illustration of normal grating lens vs. tapered grating lens is shown in Fig. 3.2 (b)

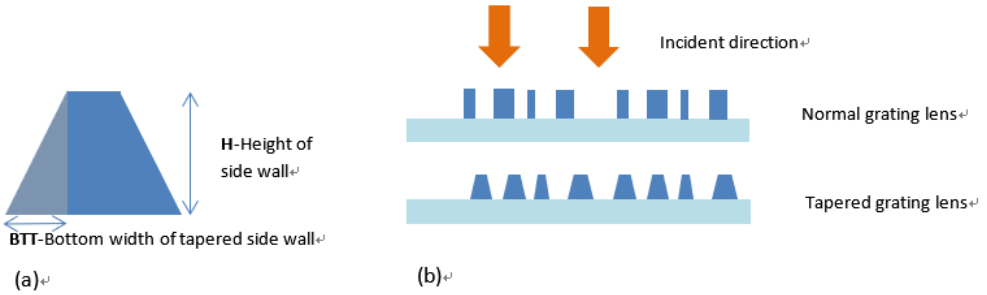

Figure 3.2. (a) Description of taper ratio. (b) Illustration of 2D cross section of normal grating lens and tapered grating lens.

Since the nano structure with tapered side wall is similar to a diminutive moth eye structure, will its transmission be enhanced? To answer this question, we pick the period of 400 nm and 450 nm (frequently used when designing micro lens) and studied its transmission when varying fill factor and taper ratio shown in Fig. 3.3.

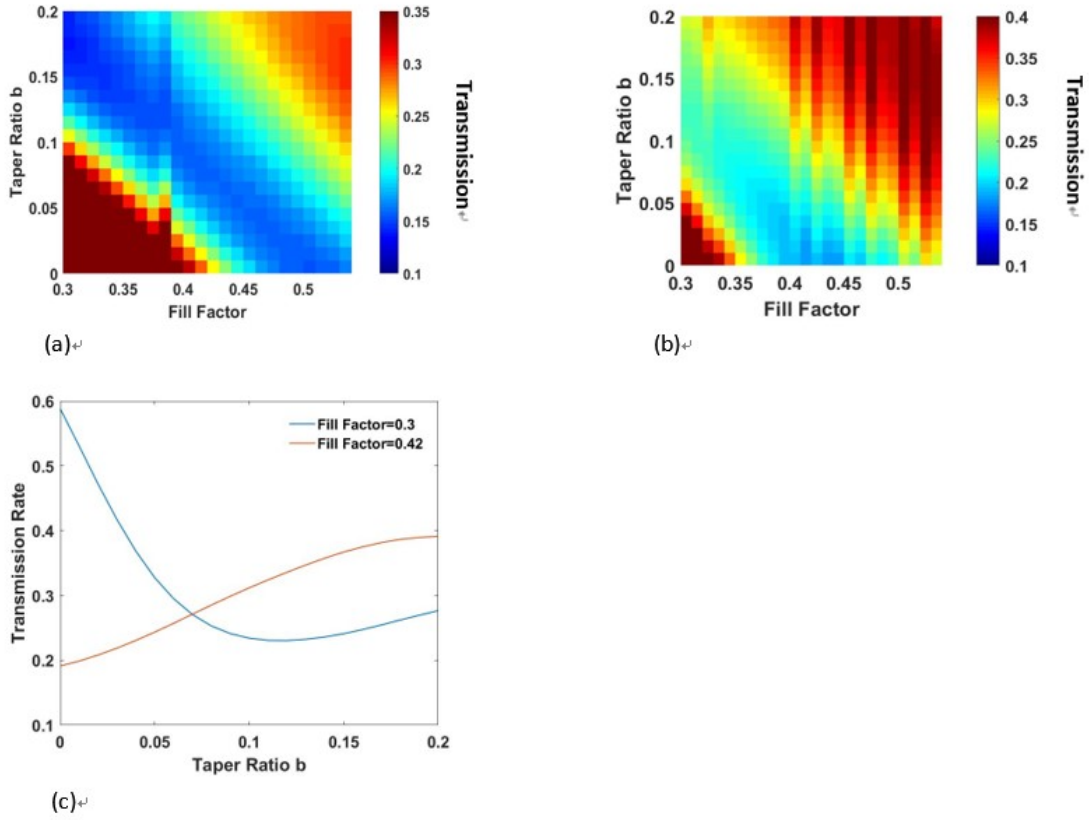

Fig. 3.3 (a) Transmission of TiO_2 phase shifter with period of 0.4 μm. (b) Transmission of TiO_2 phase shifter with period of 0.45 μm. (c) Transmission vs. Taper Ratio for phase shifter with period of 0.45 μm and fill factor of 0.3 and 0.42 respectively. The thickness of the nano structures is fixed at 400 nm.

As can be observed in Fig. 3.3 (a & b), the transmission of nano structure varies when its fill factor and taper ratio is altered. At period of 0.4 μm, for fill factor below 0.4, the transmission decreases with the increase of taper ratio. For period of 0.45 μm, same trend can be found when fill factor is below 0.35 (Fig. 3.3 b). One example is drawn in Fig. 3.3 c blue line. This is because for nano structures with low fill factor, the major area is covered by air that their high transmission is mainly resulted from low material density. The creation of taper structure on low fill factor nano structures adds a major portion of material to the original structure. As a result, the blocking effect caused by the addition of taper side wall plays a more significant role compared with the effect of transmission enhancement. On the other hand, for nano structures with fill factor larger than 0.45 (Fig. 3.3 a), the transmission increases with the increase of taper ratio. And the same trend is found for fill factor larger than 0.4 with period of 0.45 micron (Fig. 3.3 b). This indicates that, the taper enhancement effect become dominate beyond this point (fill factor of 0.45) at the period of 0.4 μm. At this point, we can conclude that, the tapered structure has transmission enhancement effect when the fill factor exceeds certain threshold. This is because the taper-blocking and taper-enhancement effect together affecting the transmission of tapered subwavelength nano structure.

While we can achieve high transmission with high refractive index material (e. g. TiO_2) in low fill factor area, we discovered that it is not possible to design a micro lens with only low fill factor nano structures. As mentioned at the beginning, the design of planar micro lens relies on a known phase matching process, thus enough phase coverage is necessary in order to form a concentrating micro lens. As shown in Fig. 3.1 b, the phase coverage is very small (less than 40 degree) for nano structures with low fill factors (e.g. less than 0.4) in a range of periods. Furthermore, low fill factor is in another word high aspect ratio, which is challenging for either etching or lift off process. To acquire enough continuous phase shift with less challenging nano fabrication for TiO_2, one group of dimensions is specified in blocks in Fig. 3.1 b and d. A micro lens with 17 phase shifters (NA=0.2) is designed within this area whose field distribution is shown as Fig. 3.4 (a) in 2D. The thickness of phase shifters is 400 nm and the lens is mounted on a glass substrate with thickness of 2 μm.

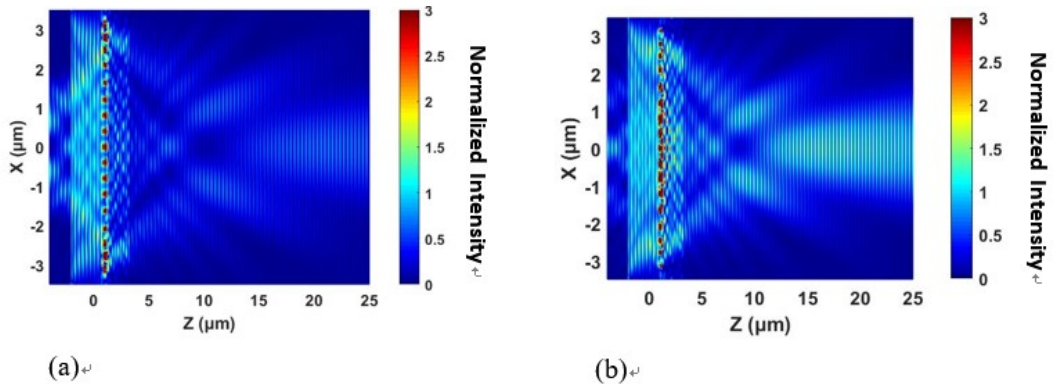

Fig. 3.4 (a) Field distribution of normal TiO_2 micro lens. (b) Field distribution of a 'tapered' TiO_2 micro lens. The intensity is normalized by incident intensity.

As shown in Fig. 3.4 (a), the lens has a very weak focus, this is because most of its phase shifters has very low transmission (0.2-0.3). As a result, reflection becomes dominant, which can also be observed in Fig. 3.1 (d). Instead of being a focusing lens, this lens become more of a reflector as the reflected power collected is around 64% of incident power.

The good news is, based on our study, it is possible that these phase shifters' transmissions be enhanced through the addition of tapered structure as all phase shifters utilized here show an increase of transmission with the growth of taper ratio.

To test the transmission enhancement of tapered structure on micro lens, a taper side wall with ***b***=0.15 is added to every phase shifter of the micro lens presented in Fig. 3.4 (a). The field distribution of taper enhanced micro lens is shown in Fig. 3.4 (b). As can be observed for tapered micro lens, a focus is formed at approximately the same place with none tapered lens (Fig. 3.4 a), while the intensity is increased by ~2.5 times.

The reflected power is reduced from ~64% to ~38%, and the focus efficiency with 2 μm width (sensor is placed at the focus point with width of 2 μm) is increased from 9% to 28%. This shows that the lens's transmission is significantly enhanced by the tapered structure which brings huge improvement of its focus property. Another point one has to be aware that the addition of tapered structure may bring extra phase shift to a nano structure which sometimes cause significant destructive effect to the focus performance if not designed in the taper resistant area. For the design

in Fig. 3.4 (b), most of the tapered structure are ‘taper resistant’ which means the extra phase introduced by taper side wall is very small that may not cause a major phase mismatch.

3.3 Conclusion

In summary, it is numerically demonstrated that a nano scale tapered structure can enhance the light transmission for phase shifters made from high refractive material. A subwavelength-grating lens is designed to examine the transmission enhancement effect.

As observed, the focus performance can be significantly increased by tapered structure. This is due to the increased transmission for each independent phase shifters. This result is not only important for the optimization of planar micro grating lens but also important for the design of micro-nano diffractive optical devices utilizing materials with high refractive index.

References

1.S. Jahani and Z. Jacob: All dielectric metamaterials. *Nature Nanotechnology* **11**, 23-36 (2016).

2.C. J. Chang-Hasnain: High-contrast gratings as a new platform for integrated optoelectronics. *Semicond. Sci. Technol* **26**, 014043 (2011).

3.S. He, Z. Wang, Q. Liu, and W. Wang: Study of focal shift effect in planar GaN high contrast grating lenses. *Opt. Express* **23**, 29360-29368 (2015).

4.P. R. West, J. L. Stewart, A. V. Kildishev, V. M. Shalaev, V. V. Shkunov, F. Strohkendl, Y. A. Zakharenkov, R. K. Dodds, and R. Byren: All-dielectric subwavelength metasurface focusing lens. *Opt. Express* **22**, 26212-26221 (2014).

5.X. Duan, G. Zhou, Y. Huang, Y. Shang, and X. Ren: Theoretical analysis and design guideline for focusing subwavelength gratings. *Opt. Express* **23**, 2639-2646 (2015).

6.D. Fattal, J. Li, Z. Peng, M. Fiorentino, and R.G. Beausoleil: Flat dielectric grating reflectors with focusing abilities. *Nature Photonics* **4**, 466-470 (2010). F. Lu, F. G. Sedgwick, V. Karagodsky, C. Chase, and C. J. Chang-Hasnain: Planar high-numerical-aperture low-loss focusing reflectors and lenses using subwavelength high contrast gratings. *Opt. Express* **18**, 12606-12614 (2010).

7.M. Ye, Y. Yi: Influence of grating thickness in low-contrast subwavelength grating concentrating lens. *Optical Engineering* **55**, 075102 (2016).

8.Y. Wang, J. Miao, Y. Tian, C. Guo, J. Zhang, T. Ren, and Q. Liu: TiO_2 micro-devices fabricated by laser direct writing. *Opt. Express* **19**, 17390-17395 (2011).

9.A. Asadollahbaik, S. A. Boden, M. D. B. Charlton, D. N. R. Payne, S. Cox and D. M. Bagnall: Reflectance properties of silicon moth-eyes in response to variations in angle of incidence, polarization and azimuth orientation. *Opt. Express* **22**, A402-A415 (2014).

10.P. Pignalosa, B. Liu, H. Chen and Y. Yi: Giant light extraction enhancement of medical imaging scintillation materials using bio inspired integrated nano structures. *Optics Letters* **37**, 2808 (2012).

11.F. Saffih, C. Con, A. Alshammari, M. Yavuz, and B. Cui: Fabrication of silicon nano structures with large taper angle by reactive ion etching. *J. Vac. Sci. Technol. B* **32,** 06FI104-1 (2014).

12.Mao Ye and Ya Sha Yi: Subwavelength grating microlens with taper-resistant characteristics.

13.M. Ye, Y. Yi: Influence of grating thickness in low-contrast subwavelength grating concentrating lens. *Optical Engineering* **55**, 075102 (2016).

14. T. Huberta, L. Boon-Brettb, G.Blackb, U. Banacha, "Hydrogen sensors – A review," Sensors and Actuators B: Chemical, vol.157, pp.329-352, Oct. 2011

15. Minghong Yang, Jixiang Dai, "Fiber Optic Hydrogen Sensors: a Review", Photonic Sensors, Volume 4, Issue 4, pp 300-324, Dec 2014

16. G. Jonsson, L. Gorton, "An electrochemical sensor for hydrogen peroxide based on peroxidase adsorbed on a spectrographic graphite electrode," Anal. Chim. Acta, vol.1, pp.465-468, Sep. 1989

17. F. Favier, E. C. Walter, M. P. Zach, T. Benter, T. R. M. Penner, "Hydrogen sensors and switches from electrodeposited palladium mesowire arrays," Science, vol. 293, pp.2227-2231, Sep. 2001

18. Y. Lu,J. Li,J. Han, H.T. Ng, C.Binder, C.Partridge, M. Meyyappan, "Room temperature

methane detection using palladium loaded single-walled carbon nanotube sensors,"Chem. Phys. Let., vol. 391, pp.344-348, Jun. 2004

19. F. Song , A. L. Garner , and K. Koide, "A Highly Sensitive Fluorescent Sensor for Palladium Based on the Allylic Oxidative Insertion Mechanism,"J. Am. Chem. Soc, vol. 129, pp.12354-12355, Sep. 2007

20. B.P. Luther, S.D.Wolter, S.E.Mohney, "High temperature Pt Schottky diode gas sensors on n-type GaN," Sens.Actu. B: Chem, vol. 56, pp.164-168, Jul, 1999

21. L. Wang, E. Wang,"A novel hydrogen peroxide sensor based on horseradish peroxidase immobilized on colloidal Au modified ITO electrode," Elec.Comm, vol. 6, pp. 225-229, Feb, 2004

22. F. D. Jr, I. S. Chen, P Chen, J. Neuner, A.Roerhla, J. Welcha, "MEMS-based hydrogen gas sensors," Sens.Actu. B: Chem, vol. 117, pp.10-16, Sep, 2006

23.A.Haddadpour and Y. Yi, "Metallic nanoparticle on micro ring resonator for bio optical detection and sensing,"Biomedical OpticsExpress, vol. 1, pp.378-384, Sep.2010

24. M. Ostrowski, P. Pignalosa and Y. Yi, "Higher order optical resonance node detection of integrated disk micro resonator," Opt. Lett., vol.36, pp.3042-3044, Aug. 2011

25. E. Krioukov, D. J. W. Klunder, A. Driessen, J. Greve, and C.Otto, "Sensor based on an integrated optical microcavity," Opt. Lett. vol. 27, pp.512-514, Apr. 2002

26. L. Goddard, K. Y. Wong, A. Garg, E. Behymer, G. Cole, and T. Bond, "Measurements of the complex refractive index of Pd and Pt films in air and upon adsorption of H2 gas,"Proceedingsof IEEE CLEO/LEOS 2008

27. A. Hessel and A. A. Oliner, "A new theory of Wood's anomalies on optical gratings,"Appl.

Opt., vol. 4, no. 10, pp. 1275–1297, Oct. 1965.

28.S. S. Wang, R. Magnusson, J. S. Bagby, and M. G. Moharam, “Guided-mode resonances in planar dielectric-layer diffraction gratings,” J. Opt. Soc. Amer. A, vol. 7, no. 8, pp. 1470–1474, Aug. 1990.

29. C. J. Chang-Hasnain and W. Yang, “High-contrast gratings for integrated optoelectronics,” Adv. Opt. Photon., vol. 4, no. 3, pp. 379–440, Sep. 2012.

30. C. F. R. Mateus, M. C. Y. Huang, Y. Deng, A. R. Neureuther, and C. J. Chang-Hasnain, “Ultrabroadband mirror using low-index cladded subwavelength grating,” IEEE Photon. Technol. Lett., vol. 16, no. 2, pp. 518–520, Feb. 2004.

31. Z. S. Liu, S. Tibuleac, D. Shin, P. P. Young, and R. Magnusson, “High- efficiency guided-mode resonance filter,” Opt. Lett., vol. 23, no. 19, pp. 1556–1558, Oct. 1998.

32. A. Szeghalmi, E. B. Kley, and M. Knez, “Theoretical and experimental analysis of the sensitivity of guided mode resonance sensors,” J. Phys. Chem. C, vol. 114, no. 49, pp. 21150–21157, Dec. 2010.

33. S. F. Lin et al., “A model for fast predicting and optimizing the sensitiv- ity of surface-relief guided mode resonance sensors,” Sens. Actuators B, Chem., vol. 176, no. 1, pp.1197–1203, Jan. 2013.

34.Y.-R. Lin, K. Y. Lai, H.-P. Wang, and J.-H. He, “Slope-tunable Si nanorod arrays with enhanced antireflection and self-cleaning proper- ties,” Nanoscale, vol. 2, no. 12, pp. 2765–2768, Dec. 2010.

35. Y. Wang et al., “Biomimetic corrugated silicon nanocone arrays for self- cleaning antireflection coatings,” Nano Res., vol. 3, no. 7, pp. 520–527, Jul. 2010.

36. K. B. Crozier, A. Sundaramurthy, G. S. Kino, and C. F. Quate, “Optical antennas: Resonators for local field enhancement,” J. Appl. Phys., vol. 94, no. 7, pp. 4632–4642, Oct. 2003.

37. A. V. Kabashin et al., “Plasmonic nanorod metamaterials for biosens- ing,” Nature Mater., vol. 8, no. 11, pp. 867–871, Oct. 2009.

38. R. Magnusson, “Wideband reflectors with zero-contrast gratings,” Opt. Lett. 39, 4337 (2014).

39.S. Wang, K. Broderick, H. Smith, and Y. Yi, “Strong coupling between on chip notched ring resonator and nanoparticle”, Applied Phys. Letter, Vol. 97, pp 051102_1-051102_3, Aug 2010

40.Ostrowski M, Pignalosa P, Smith H, Yi Y, “Higher-order optical resonance node detection of integrated disk microresonator”, Optics letters, vol. 36(16), pp. 3042-3044, Aug.2011

41.Betzig EJ, Trautman JK, Harris TD, Weiner JS, “Kostelak RL. Breaking the diffraction barrier- optical microscopy on a nanometric scale”, Science, 251(5000), pp. 1468-1470, Mar 1991

42.Suzuki, Senichi, Kazuhiro Oda, and Yoshinori Hibino, “Integrated-optic double-ringresonators with a wide free spectral range of 100 GHz”, Journal of lightwave Tech., vol. 13(8), pp. 1766-1771, Aug. 1995

43.Lee, Mindy R., and Philippe M. Fauchet, “Nanoscale microcavity sensor for single particle detection”, vol. 32, no. 22, pp.3284-3286, Nov. 2007

44.Ostrowski M, Pignalosa P, Smith H, Yi Y, “Higher-order optical resonance node detection of integrated disk microresonator”, Optics letters, vol. 36(16), pp. 3042-3044, Aug. 2011

45.Nie, Shuming, and Steven R. Emory, “Probing single molecules and single nanoparticles by surface-enhanced Raman scattering”, Science, vol. 275(5303), pp. 1102-1106, Mar. 1997

46.Va, C., Julio Montalvo, and Pedro C. Lallana, “Radio-frequency ring resonators for self-referencing fiber-optic intensity sensors”, Optical Engineering, vol. 44(4), pp. 040502_1-040502_2, Apr. 2005

47.Heijne, E.H., Jarron, P., Olsen, A. and Redaelli, N., “The silicon micropattern detector: a dream?”, Nuclear Instruments and Methods in Physics Research Section A: Accelerators, Spectrometers, Detectors and Associated Equipment, vol. 273(2), pp.615-619, Dec. 1988

48.Rafizadeh D, Zhang JP, Hagness SC, Taflove A, Stair KA, Ho ST, Tiberio RC“Waveguide-coupled AlGaAs/GaAs microcavity ring and disk resonators with high finesse and 21.6-nm free spectral range”, Optics Letters, vol. 22(16), pp. 1244-1246, Aug. 1997

Publication

1. Mao Ye, Xiaopeng Guo and Yasha Yi, “Transmission Enhancement of Subwavelength Grating Micro Lens by Tapered Nano Structure” MRS Communication”, submitted.